

TurbuGAN: An Adversarial Learning Approach to Spatially-Varying Multiframe Blind Deconvolution with Applications to Imaging Through Turbulence

Brandon Y. Feng*, Mingyang Xie*, Christopher A. Metzler

Abstract

We present a self-supervised and self-calibrating multi-shot approach to imaging through atmospheric turbulence, called TurbuGAN. Our approach requires no paired training data, adapts itself to the distribution of the turbulence, leverages domain-specific data priors, and can generalize from tens to thousands of measurements. We achieve such functionality through an adversarial sensing framework adapted from CryoGAN [1], which uses a discriminator network to match the distributions of captured and simulated measurements. Our framework builds on CryoGAN by (1) generalizing the forward measurement model to incorporate physically accurate and computationally efficient models for light propagation through anisoplanatic turbulence, (2) enabling adaptation to slightly misspecified forward models, and (3) leveraging domain-specific prior knowledge using pretrained generative networks, when available. We validate TurbuGAN on both computationally simulated and experimentally captured images distorted with anisoplanatic turbulence.

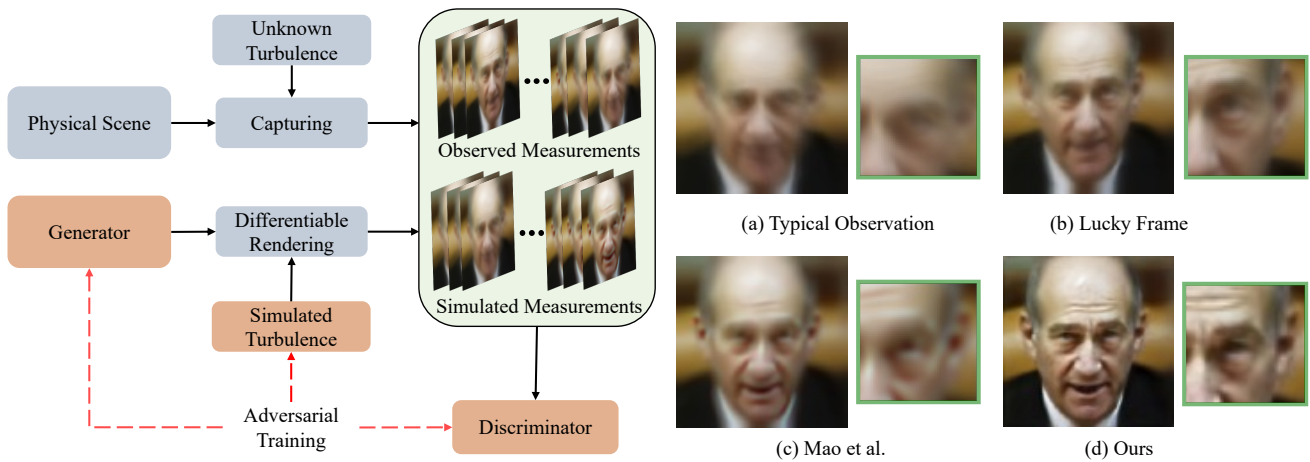


Fig. 1: TurbuGAN Framework and Reconstructions. Capturing images through turbulence often leads to highly distorted and blurry observations (a). While some individual “lucky” frames (b) may be sharper than others, one still needs to combine information from many frames to accurately reconstruct the scene. TurbuGAN (left) uses a collection of distorted measurements and produce reconstructions (d) that are sharper and contain fewer artifacts than the state-of-the-art method (c). TurbuGAN achieves this using adversarial sensing: A generator serves as the neural representation of the distortion-free scene, whose output is fed into a physically accurate and differentiable rendering engine that models the effects of atmospheric turbulence to produce simulated measurements. A discriminator compares the distribution of these measurements with the distribution of true observations of the scene. The discriminator’s feedback is used to update the generator (and optionally the turbulence simulator). The scene is finally reconstructed when the simulated measurements become indistinguishable from the true observations.

Index Terms

Adversarial training, multiframe blind deconvolution, atmospheric turbulence.

*Equal Contributions. All authors are with the Department of Computer Science, University of Maryland, College Park, MD, 20742, USA (e-mail: {yfeng97, mingyang, metzler}@umd.edu). This work was supported in part by the AFOSR Young Investigator Program.

I. INTRODUCTION

Atmospheric turbulence causes long-range imaging systems to capture blurry and distorted measurements. These distortions are caused by the heterogeneous refractive index of the atmosphere: When light propagates through the atmosphere, this heterogeneity will induce spatially-varying phase delays in the wavefront, which in turn determines the optical system's point spread function (PSF). When the heterogeneity is distributed over a volume, the turbulence is said to be anisoplanatic and the PSF is spatially-varying. Accordingly, imaging through anisoplanatic turbulence can be described by the equation

$$\mathbf{y}_i(u, v) = \mathbf{h}_i(u, v) * \mathbf{x} + \boldsymbol{\epsilon}_i, \quad (1)$$

where (u, v) are pixel coordinates, $\mathbf{y}_i \in \mathbb{R}^{N \times N}$ is an observed blurry image, $\mathbf{h}_i(u, v) \in \mathbb{R}^{M \times M}$ is a spatially-varying blur kernel at location (u, v) , $\mathbf{x} \in \mathbb{R}^{N \times N}$ is the target being imaged, $\boldsymbol{\epsilon}_i \in \mathbb{R}^{N \times N}$ is (possibly signal dependent) noise, N is the image size in pixels, and M is the kernel size in pixels. When imaging a stationary target through dynamic turbulence, the signal \mathbf{x} is fixed while at each time step the measurements $\mathbf{y}_1, \mathbf{y}_2, \dots, \mathbf{y}_L$ experience different blur kernels $\mathbf{h}_1, \mathbf{h}_2, \dots, \mathbf{h}_L$.

The central challenge posed by the forward model described by Equation (1) is that the underlying turbulence is *stochastic* across different locations and instances of time. Without prior information or measurements such as a guiderstar [2], the spatially-varying blur kernels $\{\mathbf{h}_i\}_{i=1}^L$ are unknown and recovering \mathbf{x} requires solving a spatially-varying multiframe blind deconvolution problem.

To tackle this problem, classical algorithms often explicitly estimate or marginalize over the latent variables (blur kernels) which characterize the turbulence associated with each measurement. Such strategies are computationally intensive and impractical when the turbulence is spatially-varying and/or the number of measurements becomes large. Alternatively, one can train an application-specific deep neural network to reconstruct sharp images from distorted measurements. However, such networks rely on large quantities of representative training data and cannot be easily adapted to new turbulence models at test time.

A. Contributions

We develop a new self-supervised spatially-varying multiframe blind deconvolution algorithm for imaging through atmospheric turbulence. The proposed algorithm uses an adversarial sensing framework shown in Fig. 1, in which a neural representation of a scene and a physically-accurate differentiable forward model are combined to generate synthetic measurements. A discriminator network is then used to compare the *distributions* of the synthesized and experimental measurements to provide a feedback signal that improves the quality of synthesized measurements. Adversarial sensing, which was first developed for unknown-view-tomography in the context of single-particle cryogenic electron microscopy (cryo-EM) [1], is explained in detail in Section III.

To our knowledge, this is the first application of adversarial sensing to multiframe blind deconvolution or imaging through atmospheric turbulence. By leveraging adversarial sensing, TurbuGAN provides several distinct advantages over previous methods. Unlike classical algorithms, TurbuGAN requires neither reconstructing nor marginalizing over the latent variables which characterize the turbulence associated with each measurement. Unlike supervised deep learning methods, TurbuGAN does not rely on a large corpus of paired training data and is thus robust to out-of-distribution test data or turbulence strengths. Moreover, while many (but not all, *e.g.* [3]) supervised deep learning methods make predictions based on a fixed numbers of input frames in a single-shot fashion, TurbuGAN is able to iteratively refine its prediction given an arbitrary number of measurements.

Our largest contributions can be summarized as follows.

- 1) We present a novel adversarial sensing framework for the problem of multiframe imaging through anisoplanatic turbulence.
- 2) We demonstrate adversarial sensing can be combined with off-the-shelf generative networks (*e.g.* StyleGAN [4] and StyleGAN-XL [5]) to impose strong but specialized priors on the reconstructed images.

- 3) We demonstrate adversarial sensing can be combined with untrained generative networks (*e.g.* DIP [6]) to impose weak but flexible priors on the reconstructed images.
- 4) We extend adversarial sensing to deal with misspecified forward model and show that this extension allows us to adapt to unknown turbulence conditions.
- 5) We validate our method on both computationally simulated and experimentally captured data.

B. Limitations

While our work represents a fundamentally new approach to imaging through turbulence, it does come with a few notable limitations. First, our current work assumes we have multiple measurements of a static object and does not currently support dynamic scenes. Second, our method is computationally expensive: reconstructing a 128×128 image from 2,000 distorted observations takes around three hours on a single GPU (Nvidia RTX A6000).

II. RELATED WORK

A. Imaging Through Turbulence

Over the past three decades, many multiframe blind deconvolution and turbulence-removal algorithms have been developed. The oldest and most widely used approach to multiframe imaging through turbulence is lucky imaging. Lucky imaging is founded on the concept that even under moderately severe turbulence conditions, given a large number of measurements, there is a high probability that at least one measurement will experience very little turbulence-induced distortion [7]. Likewise, modern anisoplanatic turbulence removal algorithms [8] often extract the lucky patches from an image sequence as an important step during the registration process. Nonetheless, lucky imaging provides limited benefits when all the measurements are blurry and there are no lucky frames to take advantage of.

When all the images in the sequence are blurry, one likely needs to perform deconvolution explicitly. Expectation-maximization (EM) based deconvolution algorithms reconstruct the image while marginalizing over the distribution of the blur kernels [9]. However, the computation cost of EM-based methods scales exponentially with the number of latent variables, making it impractical to deploy in applications involving high-dimensional continuous latent variables (*i.e.*, high-resolution spatially-varying blur kernels).

A simpler alternative to EM is alternating minimization (AM). AM-based deconvolution algorithms attempt to reconstruct both the blur kernels and the image by imposing various priors on each. For instance, in [10] the authors impose a sparse total variation prior on the image and a sparse and positive constraint on the blur kernels. Recent efforts have imposed more accurate models on the images (non-local self-similarity [11]) and the blur kernels (Kolmogorov turbulence) [8]. To our knowledge, the method developed in [8] represents the current state-of-the-art in multiframe imaging through turbulence.

Deep learning provides the possibility to develop turbulence removal algorithms that benefit from a large amount of training data. Several recent works have trained deep neural networks to remove atmospheric distortions from a single image [12]–[14]. Recently, Mao et al. [15] trained a convolutional neural network to reconstruct a sharp image from 50 frames degraded by atmospheric turbulence. Their method achieved performance only incrementally worse than state-of-the-art classical methods while running significantly faster. For more traditional blind deconvolution tasks, like removing camera shake, researchers have developed methods [3], [16] that generalize across an arbitrary number of frames. All these methods train their network to a specific blur kernel family or turbulence level, limiting their adaptability.

B. Imaging Inverse Problem with Generative Networks

By constraining reconstructed images to lie within the range of a deep generative network and then finding the latent parameters consistent with the measurements, several research groups have solved under-determined imaging inverse problems such as compressive sensing [17]–[22] and phase retrieval [23]–[25]. As shown in Deep Image Prior (DIP) [6], a similar framework can be effective even if the generative network is untrained.

By estimating both the object and unknown forward model, this framework can be adapted to problems with unknown forward models, such as blind demodulation [26], blind deconvolution [27], [28], phase retrieval with optical aberrations [29], and blind super-resolution [30]. However, such approaches, which largely boil down to alternating minimization with respect to both the scene’s and forward model’s latent spaces, do not easily apply to our multiframe anisoplanatic turbulence removal problem because they would require reconstructing all the blur kernels associated with all the pixels of all the observations.

C. CryoGAN

CryoGAN [1] similarly reconstructs images by fitting a network to a collection of measurements, but it does so using a fundamentally different approach which compares the *distributions* of simulated and real observations. We refer to this approach as adversarial sensing.

In CryoGAN, adversarial sensing compares the distributions of simulated and real tomographic projections and updates the underlying reconstruction so that those two distributions become more homogeneous. Since the network is fitted over entire distributions, not individual observations or predictions, adversarial sensing allows one to perform reconstruction even when one-to-one correspondence between an observation and its associated latent variables cannot be established. In the context of cryo-EM, this challenge arises because the latent orientation associated with each observed projection of the 3D object (molecule) is highly under-determined. In this work, we extend adversarial sensing to the task of turbulence removal.

III. METHODS: ADVERSARIAL SENSING

Our goal is to recover the underlying target scene \mathbf{x} given a set of observations $\{\mathbf{y}_i\}_{i=1}^L$, characterized by the equation

$$\mathbf{y}_i(u, v) = \mathbf{h}_i(u, v) * \mathbf{x} + \epsilon_i, \quad (2)$$

where the set of spatially-varying blur kernels $\{\mathbf{h}_i\}_{i=1}^L$ are unknown. We approach this challenging blind deconvolution problem with adversarial sensing.

Our framework is illustrated in Fig. 1. An either pre-trained [4], [5] or randomly initialized [6] generator network \mathcal{G}_θ takes in a fixed input \mathbf{z} and produce a single image $\tilde{\mathbf{x}}$, which serves as the estimated reconstruction of the distortion-free scene. This reconstruction is fed to a physics-based differentiable forward model which synthesizes distorted measurements, $\mathbf{h} * \tilde{\mathbf{x}}$. These synthesized measurements are then sent to a discriminator, which is trained to differentiate these synthetic measurements from the real observations, $\mathbf{h} * \mathbf{x}$. In effect, the discriminator provides a loss on how close the synthesized data’s distribution, $p_{h*\tilde{x}}(\mathbf{y})$, is to the true data’s distribution, $p_{h*\mathbf{x}}(\mathbf{y})$. The discriminator loss is used to update the generator network’s weights θ so as to improve its reconstruction $\tilde{\mathbf{x}}$ until $p_{h*\tilde{x}}(\mathbf{y})$ and $p_{h*\mathbf{x}}(\mathbf{y})$ are indistinguishable. We may optionally back-propagate the loss to the differentiable forward model and update its parameters as well.

A. Physically Accurate Differentiable Forward Model for Anisoplanatic Atmospheric Turbulence

Our framework relies upon having access to a physically accurate forward model that can simulate realistic turbulence on top of the estimate of \mathbf{x} , so that the synthetic measurements follow the same distribution as the real measurements. This forward model also needs to be differentiable to enable loss back-propagation to update the generator network \mathcal{G} .

As explained in [31], the blur kernel \mathbf{h} associated with the turbulence at location (u, v) is related to the phase errors $\phi(u, v)$ at that location via the expression

$$\mathbf{h}(u, v) = |\mathcal{F}(e^{-j\phi(u, v)})|^2. \quad (3)$$

Thus, one can generate realistic blur kernels by generating realistic phase errors $\phi(u, v)$ for all (u, v) . Specifically, at each pixel (u, v) one can approximate $\phi(u, v)$ with the first M Zernike polynomials as

$$\phi(u, v) = \sum_{i=1}^M \alpha_i Z_i(u, v), \quad (4)$$

where Z_i is the i^{th} Zernike basis and α_i is its corresponding coefficient [32]. The vector of coefficients α follows a zero-mean normal distribution with covariance matrix Σ . Detailed derivations [32], [33] show that Σ depends on the ratio of the imaging system's aperture's diameter D and the Fried parameter r_0 [7], which characterizes the turbulence strength.

The correlations between the Zernike phase errors at adjacent locations are similarly well understood [33]. Thus, to model propagation through atmospheric turbulence, one can (A) sample a collection of correlated Zernike coefficients for every image pixel, (B) use Equations (3) and (4) to compute the PSF associated with each pixel, and (C) convolve each pixel in the scene with its associated PSF [33]. As one might expect, performing these computations explicitly is extremely computationally expensive.

Fortunately, the recently proposed phase-to-space (P2S) transform [15] bypasses the computationally expensive blur kernel generation process (Equations (3) and (4)) by training a neural network to learn a mapping directly between the Zernike coefficients and blur kernels. Simulation results demonstrate that the blur kernels generated with the P2S transform are physically accurate, consistent with existing theory, and can be evaluated $300\text{--}1000\times$ faster than previous physics-based forward models [15]. Accordingly, we adopt the P2S transform both to generate the ground truth observations and serve as our differentiable rendering engine to generate the synthetic measurements during training.

B. Optimization Objectives

Adversarial sensing follows the standard adversarial learning paradigm, where one trains a generator \mathcal{G} to trick a discriminator \mathcal{D} and also trains \mathcal{D} not to get tricked. However, different than conventional GAN training, the discriminator loss is computed based on the distorted measurements, rather than the direct output of the generator.

1) *Optimizing the Discriminator*: To train the discriminator, for each training batch we first gather a collection of K observed distorted measurements \mathbf{y} . Next, we obtain the current estimated target image $\mathcal{G}(z) = \tilde{\mathbf{x}}$ and construct fake observations $\{\tilde{\mathbf{y}}_i(u, v) = \tilde{\mathbf{h}}_i(u, v) * \tilde{\mathbf{x}}\}$.

We then send both $\{\tilde{\mathbf{y}}_i\}$ and $\{\mathbf{y}_i\}$ to the discriminator to compute $\{\mathcal{D}(\mathbf{y}_i)\}$ and $\{\mathcal{D}(\tilde{\mathbf{y}}_i)\}$. Finally, we update the discriminator \mathcal{D} with loss $L_D = L_D^{real} + L_D^{fake} + L_D^{mix}$, where the three terms are defined as:

$$L_D^{real} = \frac{p_d}{K} \sum_{i=1}^K \mathcal{D}(\mathbf{y}_i)^2 - \frac{1}{K} \sum_{i=1}^K \mathcal{D}(\mathbf{y}_i), \quad (5)$$

$$L_D^{fake} = \frac{1}{K} \sum_{i=1}^K \mathcal{D}(\tilde{\mathbf{y}}_i). \quad (6)$$

$$L_D^{mix} = \frac{p_r}{K} \sum_{i=1}^K (\|\nabla_{\mathbf{b}} \mathcal{D}(\mathbf{b})\|_2 - 1)^2 \quad (7)$$

This loss function is based on the Wasserstein GAN loss [34], and p_d and p_r are both regulatory parameters. In the third term L_D^{mix} , $\mathbf{b} = \alpha \tilde{\mathbf{y}}_i + (1 - \alpha) \mathbf{y}_i$, where α are randomly sampled from $[0, 1]$. This loss term softly enforces the Lipschitz constraint on the discriminator and decreases training difficulty.

2) *Optimizing the Generator*: Optimizing the generator is straightforward. We encourage the generator to produce fake samples that are scored higher by the discriminator. The generator's loss is defined as:

$$L_G = -\frac{1}{K} \sum_{i=1}^K \mathcal{D}(\tilde{\mathbf{y}}_i). \quad (8)$$

C. Theoretical Justification

Before delving into the experimental results, we demonstrate that in the simpler case of isoplanatic turbulence (spatially-invariant blur) with a known distribution, matching the distributions of the simulated and observed noise-free measurements reconstructs the scene.

Theorem III.1. *Let $p_{h*x}(\mathbf{y})$ denote the distribution associated with noiseless spatially-invariant measurements*

$$\mathbf{y} = \mathbf{h} * \mathbf{x}, \text{ where } \mathbf{h} \sim p_h. \quad (9)$$

Let $p_{h\tilde{x}}(\mathbf{y})$ denote the distribution associated with measurements formed by a reconstruction $\tilde{\mathbf{x}}$ and blur kernels following p_h . Then,*

$$p_{h*x}(\mathbf{y}) = p_{h*\tilde{x}}(\mathbf{y}) \implies \mathbf{S} \circ |\mathcal{F}\mathbf{x}| = \mathbf{S} \circ |\mathcal{F}\tilde{\mathbf{x}}|, \quad (10)$$

where \circ denotes a Hadamard (elementwise) product, \mathcal{F} denotes the 2D Fourier transform, and $\mathbf{S} = \mathbb{1}_+(\mathbb{E}[|\mathcal{F}\mathbf{h}|^2])$ where $\mathbb{1}_+(\cdot)$ denotes an indicator function that is 1 if its argument is greater than 0.

In effect, Theorem III.1 states that if adversarial sensing can match the distributions of the observed and simulated measurements, it will reconstruct \mathbf{x} accurately up to the invariances (e.g. translation) associated with the masked phase retrieval problem defined by the right hand side of Equation (10).

Corollary III.1.1. *If one further makes the (strong) assumption that $\mathbb{E}[\mathcal{F}\mathbf{h}](K_u, K_v) \neq 0$ for all spatial frequencies (K_u, K_v) , then $\mathbf{x} = \tilde{\mathbf{x}}$.*

Proofs of Theorem III.1 and Corollary III.1.1 can be found in the Appendix.

IV. EXPERIMENTS

In this section, we perform several experiments to evaluate the proposed method on the turbulence removal problem. During all TurbuGAN training, we apply the fast simulator introduced by Mao et al. [15] to generate realistic anisoplanatic turbulence. Unless otherwise noted, in all experiments we simulate $L = 2000$ measurements for each scene with an aperture diameter D of 0.1 meters, a Fried parameter r_0 of 0.05, and a distance to target of 1000 meters. In each iteration, we use a batch size $K = 32$ for both observed and simulated measurements. All target images have a resolution of 128×128 . Both \mathbf{D} and \mathbf{G} are trained using the Adam optimizer [35]; we first warm up \mathbf{D} for 5000 iterations while fixing \mathbf{G} ; afterwards, we alternate between updating \mathbf{D} for six iterations and \mathbf{G} for one iteration. Training stops after 100,000 iterations and takes about three hours on an NVIDIA RTX A6000 GPU. Our implementation in PyTorch [36] will be released upon acceptance.

Different Priors. TurbuGAN allows us to flexibly select different strategies to initialize the neural network \mathbf{G}_θ , each imposing different levels of prior knowledge about the scene. In our experiments, we start with testing TurbuGAN on face images and then extend it to general, non-face images. Therefore, we deploy TurbuGAN under three conditions: 1) *Face*, where we have the strongest level of prior knowledge about the domain of human faces, 2) *IN* (short for ImageNet), a moderate level of prior knowledge on the domain of natural images, and 3) *DIP*, no domain-specific knowledge. For the *Face* condition, we use the weights of StyleGAN2 [4] pretrained on the FFHQ dataset [37] containing real human face images. For the *IN* condition, we use the weights of StyleGAN-XL [5] pretrained on the ImageNet dataset [38]. For the *DIP* condition, we use PyTorch’s default Kaiming initialization [39] to initialize the weights.

Initialization Schemes. Before training under the first two conditions, we first optimize the input vector z similar to the first stage of the Pivotal Tuning Inversion (PIT) approach [40], which has demonstrated state-of-the-art performance on GAN inversion. Specifically, we optimize z such that the initial generator output matches the reconstructed result of [8]. We then optimize the network weights based on the training objective described in Section III-B.

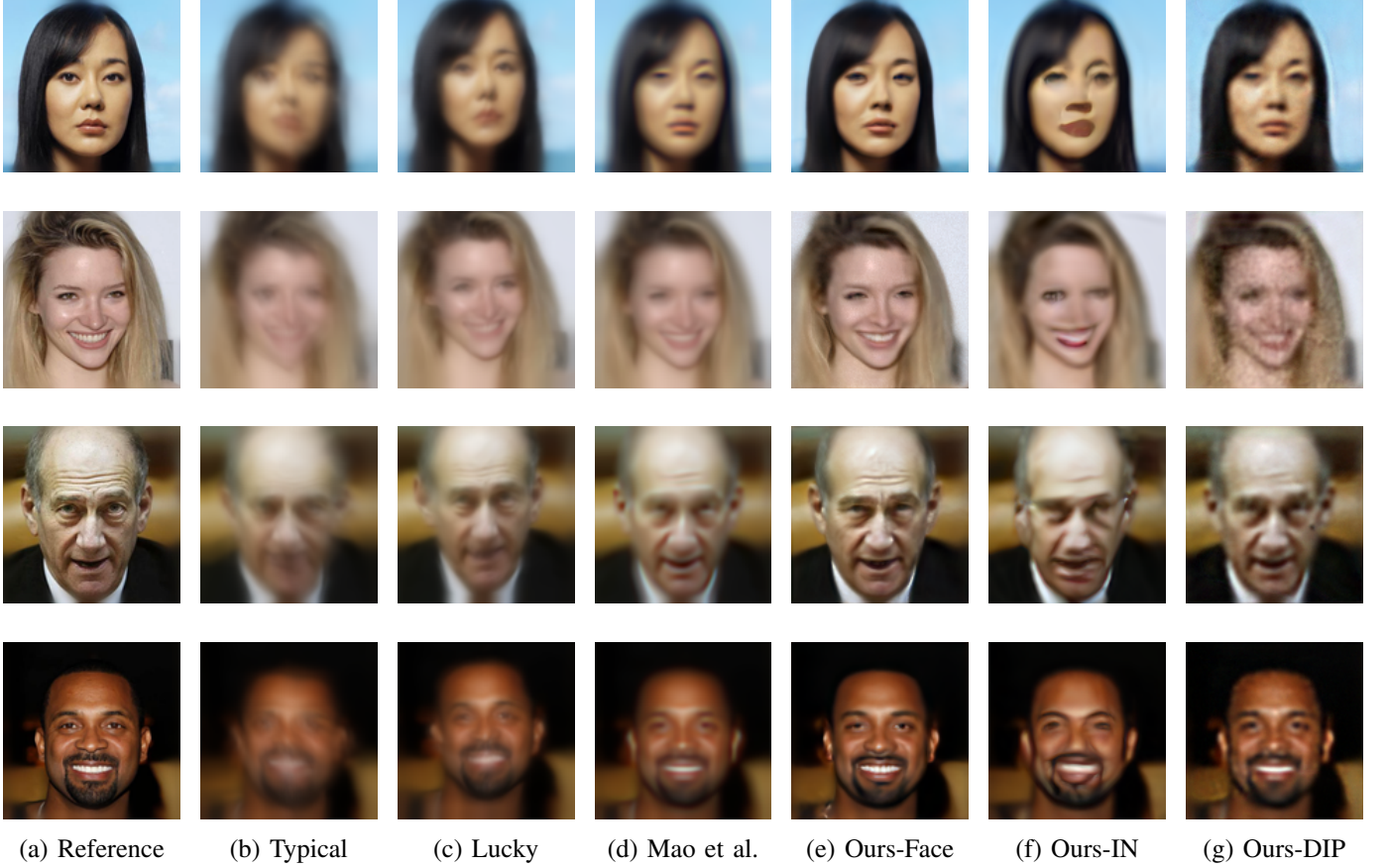


Fig. 2: Reconstructions from Simulated Turbulence-Distorted Face Images. Given the reference image (a), we simulate 2000 observations distorted by spatially-varying turbulence. Typical distorted frames are shown in (b) and handpicked lucky frames are shown in (c). The results produced by [8] are shown in (d), which are not much sharper than the lucky frames. In (e)-(f), we show reconstructions produced by TurbuGAN under three conditions (details in IV-A) with different levels of prior knowledge about the data domain (face images in this case). (e) utilize a StyleGAN generator pretrained on faces and show fine details and clear structure consistent with the reference images. (f) utilize a generator pretrained on natural images (ImageNet), while (g) assume no knowledge about the image domain by using a randomly initialized generator. Nonetheless, all conditions still achieve reasonable results, showing the flexibility of our framework in adapting to different levels of prior knowledge.

A. Results on Computationally Simulated Images

We use the P2S turbulence simulator [15] to computationally induce physically-accurate turbulence on images. The selected images include real human faces from the CelebA dataset [41], and non-face, publicly available images [42], [43] outside the ImageNet dataset [38]. We compare TurbuGAN with a state-of-the-art turbulence-removal algorithm [8] and show qualitative comparisons in Fig. 2. TurbuGAN succeeds in restoring the original image, while the baseline method produces blurry images with obvious artifacts. Results in Fig. 3 further demonstrate that TurbuGAN extends to data domains where we cannot initialize the generator with domain-specific prior knowledge.

B. Adapting to Misspecified Forward Models

In the turbulence simulator [15], the turbulence strength is described by D/r_0 , where D is the aperture diameter and r_0 is the Fried parameter [7]. In previous experiments, we set the same D/r_0 values when we generate observed and simulated measurements. However, while in real-world imaging scenarios the



Fig. 3: Reconstructions from Simulated Turbulence-Distorted General Images. We extend to general, non-face images, with experiments done under turbulence strength $D/r_0 = 2.0$. The results produced by [8], shown in (d), contain relatively few artifacts but are generally blurry. When we initialize the generator with StyleGAN generator pretrained on face images, the results (e) show some visible artifacts since the initialized weights possess a strong prior on faces. We achieve better results (g) with generator pretrained on ImageNet, which has less specialized but more flexible prior over natural images. However, the digits results (third row) contain visible artifacts since they are not natural images and fall outside of the domain of ImageNet. When using a randomly initialized generator (DIP), the reconstructions (g) are sharp and contain minimal artifacts. These results show that TurbuGAN extends beyond face images and remains robust by flexibly adapting to appropriate levels of domain-specific prior knowledge.

aperture diameter D is usually known, the Fried parameter r_0 is likely unknown. Our framework would have limited use if it required knowing the precise turbulence strength D/r_0 of the scene.

We now demonstrate TurbuGAN can be made robust to misspecified forward models by treating D/r_0 as a learnable parameter. To analyze the impact of learning to update D/r_0 in the simulator, we initialize the simulator with various D/r_0 values and then compare the final performance when one learns or fixes the D/r_0 parameter. In this set of experiments, we select the same face image as the target and set the true unknown $D/r_0 = 2$ and test under five conditions with different initial D/r_0 ranging from 1 to 5.

In Fig. 4, we plot the final reconstruction quality (measured in PSNR) against different misspecified

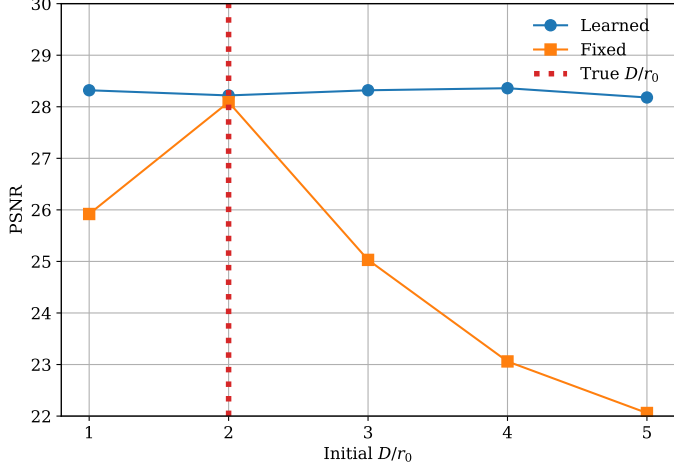


Fig. 4: **Adapting to Mismatched Turbulence Strength D/r_0 .** We set the true unknown turbulence strength level D/r_0 equal to 2 (red vertical line). We initialize our framework with different D/r_0 levels ranging from 1 to 5, and we compare the performance (PSNR) between learning and fixing the initial D/r_0 . The orange curve shows that the reconstruction quality significantly deteriorates when the framework sticks to a misspecified turbulence strength level. The blue curve shows that by updating D/r_0 during training, our method is able to overcome severe initial mismatches and achieve almost the same performance as when it is correctly initialized with $D/r_0 = 2$.

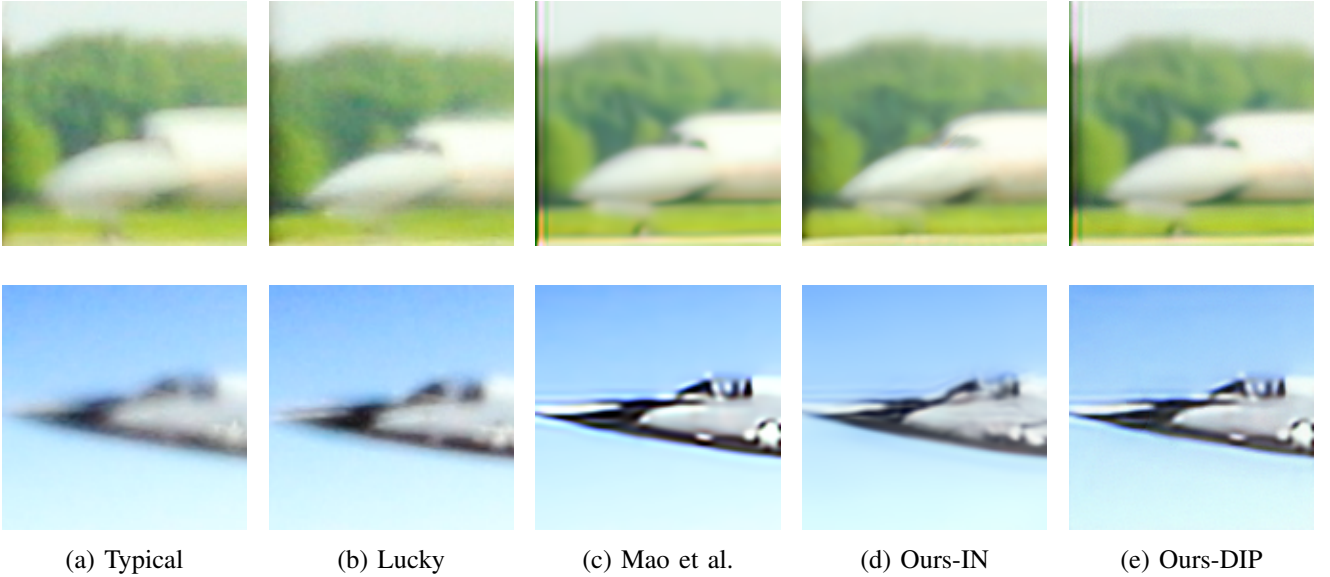


Fig. 5: **Reconstructions from Experimentally-Captured Turbulence-Distorted Images.** We further apply TurbuGAN to measurements distorted by real-world atmospheric turbulence. Each scene contains 100 measurements with unknown levels of turbulence distortion. Results show that TurbuGAN’s performance is robust on real-world data. Our reconstructions when not assuming any domain-specific priors (*DIP*) appear sharper than when leveraging the prior from the ImageNet (*IN*) domain, as shown in (d) and (e).

initial D/r_0 . Evidently, learning to adjust the turbulence strength level D/r_0 during training overcomes the incorrect initialization (we observed the adapted turbulence strengths consistently converged to the true D/r_0) and significantly improves the reconstruction quality.

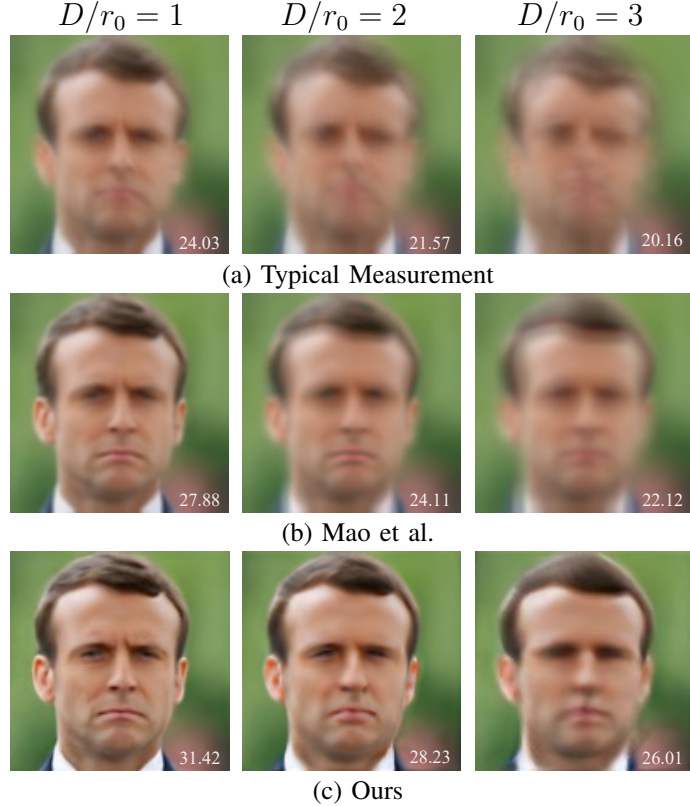


Fig. 6: Effect of Varying the Turbulence Strength D/r_0 . We compare the visual quality of a typical measurement (top row), the reconstruction by [8] (middle row), and by our method (bottom row) at 3 different D/r_0 levels from left to right. We present the PSNR at the bottom right of each image. TurbuGAN outperforms Mao et al. [8] at all 3 turbulence strengths with sharper and more accurate reconstructions.

C. Results on Experimentally Captured Images

For the experimentally-captured setting, we use images from the dataset provided by CVPR 2022 UG2 Challenge: Atmospheric Turbulence Mitigation [44]. These images are captured by the providers with turbulence generated in a real-world environment using heated hot air.

Since the levels of turbulence strength are unknown for these data, we jointly learn to adjust our simulated turbulence strength level D/r_0 along side with the networks. Reconstruction from these experimentally-captured data in Fig. 5 demonstrate that Turbogan is able to recover images from real-world turbulence as well, though in the case of real turbulence the reconstructions are not appreciably better than [8]. (No ground-truth is provided.)

V. ANALYSIS AND DISCUSSION

In this section, we present further analysis on how varying different attributes of the problem setting affect TurbuGAN’s performance. Additionally, we discuss the implications of our method.

Different Turbulence Levels. We assess TurbuGAN on different levels of difficulty by varying the strength of turbulence when simulating the blurry measurements. Fig. 6 demonstrates that TurbuGAN consistently outperforms [8] across a variety turbulence levels.

Distribution Matching. As noted in Section III-C, TurbuGAN’s reconstruction capabilities hinge on its ability to successfully match the observed and simulated distributions. In Fig. 7, we demonstrate that during adversarial training, the distribution of the simulation measurements gradually becomes indistinguishable from the true measurements’ distribution. Fig. 8 highlight how the reconstruction quality improves as TurbuGAN learns to improve the distribution of simulated measurements. We do not use early stopping

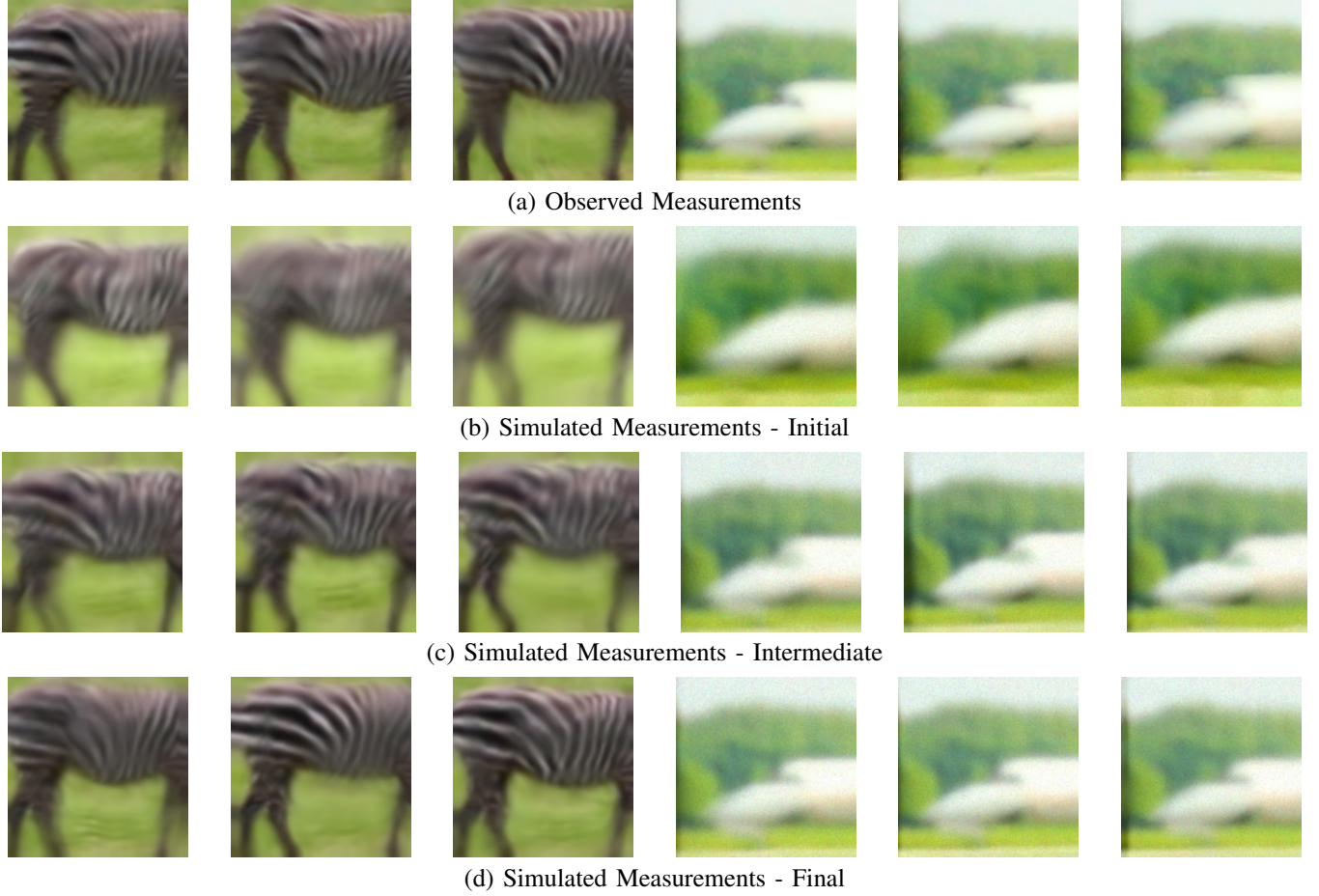


Fig. 7: Comparison Between the Distribution of Synthesized and Observed Measurements. We show randomly selected frames from the observed measurements (a), simulated measurements at network initialization (b), simulated measurements at an intermediate iteration (c), and simulated measurements at the final iteration (d). The distribution of the simulated measurements (b)-(d) become increasingly similar to the distribution of the observed measurements (a) over time. The zebra observations (left) are synthetic while the airplane observations (right) were experimentally captured. TurbuGAN gradually matches the distributions of both datasets.

since we consistently observe that as the number of iterations increases, the reconstruction quality steadily improves in terms of both visual quality and quantitative metrics such as PSNR.

Measurement Usage. Among learning-base methods, TurbuGAN is somewhat unique in its ability to take advantage of an arbitrary number of measurements. As demonstrated in Fig. 9, TurbuGAN’s reconstruction quality increases with the number of available measurements. While our method can produce reasonable reconstructions using only 20 measurements, the more it has the better it does.

Connections to EM. Although the well-known EM algorithm can be also regarded as comparing the distributions of real and simulated measurements, in EM this comparison is performed explicitly using analytic expressions, rather than implicitly with a discriminator. Accordingly, EM requires one to discretize the distribution of the latent variables (to make marginalization computationally feasible). EM also requires analytically maximizing the log likelihood of measurements, often resulting in a Gaussian assumption on the noise, which turns the log-likelihood maximization problem into a easy-to-solve least-squares problem. Unfortunately, EM does not scale to high dimensional latent variables. For example, even with 15 Zernike coefficients each discretized into only 5 bins, each E step of the EM algorithm would require computing 5^{15} potential measurements per image! Modeling anisoplanatic turbulence is significantly harder still.

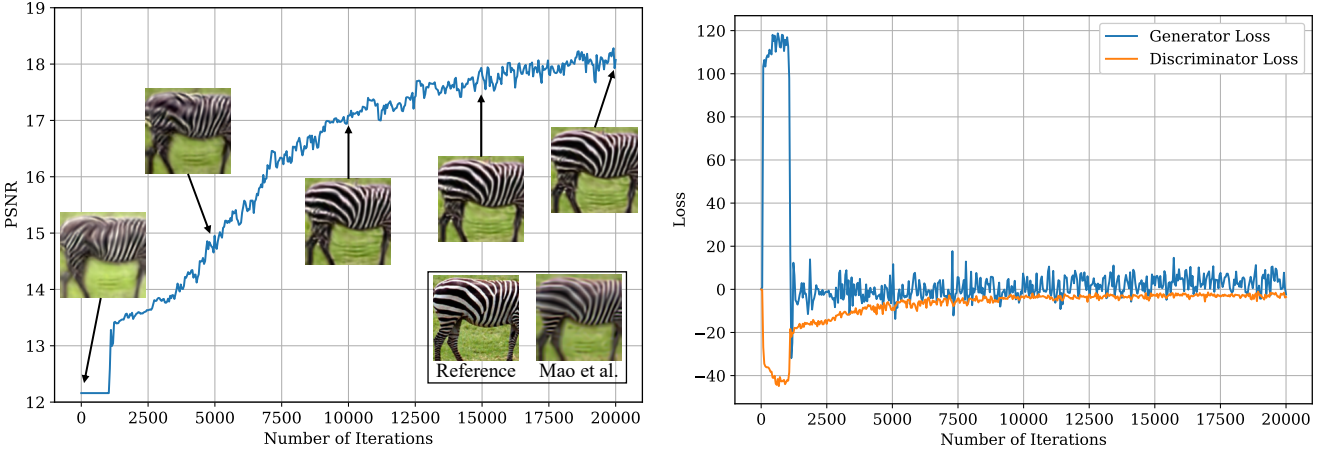


Fig. 8: Reconstruction Improves During Training. For the scene shown in Figure 7, we additionally plot the PSNR (left) and training losses (right). In the left, we also display the initial generator output and the reconstructions as training progresses. The reference ground truth image and the reconstruction by [8] are placed at the lower right corner for comparison. Both the visual quality and PSNR steadily improve over time. In the right, we present the loss curves for both the generator and the discriminator, showing that the two networks gradually reach a stalemate where neither can improve much further.

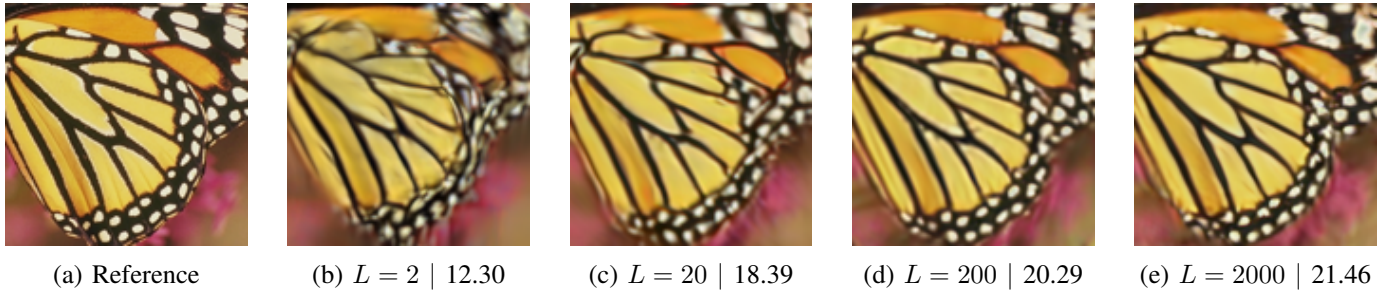


Fig. 9: Varying the Number of Measurements L . We deploy TurbuGAN with varying number of observations under simulated turbulence strength $D/r_0 = 1.5$. TurbuGAN benefits from more observations: Both the visually quality and the PSNR of the reconstructions (displayed next to L) improves as L increases.

TurbuGAN avoids the high computational complexity of the EM algorithm and is able to reconstruct the scene without explicitly solving for the continuous latent variables associated with each measurement.

VI. CONCLUSION

This work introduces TurbuGAN, a spatially-varying multiframe blind deconvolution method based on the adversarial sensing concept [1]. TurbuGAN is able to effectively synthesize thousands of highly distorted images, each modeling the effects of severe atmospheric turbulence, into a single high-fidelity reconstruction of a scene. While TurbuGAN’s performance is especially strong in domains where it has access to prior information (via a pretrained generative network), when combined with untrained networks, TurbuGAN is also surprisingly effective in domains where no such priors are available. Moreover, TurbuGAN can adapt to misspecified forward models.

Adversarial-sensing-based reconstruction methods, like TurbuGAN, represent a fundamentally new approach to solving inverse problems in imaging. They open up the possibility of applying deep learning to tackle previously unsolvable inverse problems in imaging where limited or no training data is available and only the distribution of the forward measurement model is known.

REFERENCES

- [1] H. Gupta, M. T. McCann, L. Donati, and M. Unser, "CryoGAN: A New Reconstruction Paradigm for Single-Particle Cryo-EM Via Deep Adversarial Learning," *IEEE Transactions on Computational Imaging*, vol. 7, pp. 759–774, 2021.
- [2] J. M. Beckers, "Adaptive Optics for Astronomy: Principles, Performance, and Applications," *Annual Review of Astronomy and Astrophysics*, vol. 31, no. 1, pp. 13–62, 1993.
- [3] M. Aittala and F. Durand, "Burst Image Deblurring Using Permutation Invariant Convolutional Neural Networks," in *Proceedings of the European Conference on Computer Vision (ECCV)*, 2018, pp. 731–747.
- [4] T. Karras, S. Laine, M. Aittala, J. Hellsten, J. Lehtinen, and T. Aila, "Analyzing and Improving the Image Quality of Stylegan," in *Proceedings of the IEEE/CVF Conference on Computer Vision and Pattern Recognition*, 2020, pp. 8110–8119.
- [5] A. Sauer, K. Schwarz, and A. Geiger, "StyleGAN-XL: Scaling StyleGAN to Large Diverse Datasets," in *ACM SIGGRAPH 2022*, 2022.
- [6] D. Ulyanov, A. Vedaldi, and V. S. Lempitsky, "Deep Image Prior," *2018 IEEE/CVF Conference on Computer Vision and Pattern Recognition*, pp. 9446–9454, 2018.
- [7] D. L. Fried, "Probability of Getting a Lucky Short-Exposure Image Through Turbulence," *Journal of the Optical Society of America*, vol. 68, pp. 1651–1658, 1978.
- [8] Z. Mao, N. Chimitt, and S. H. Chan, "Image Reconstruction of Static and Dynamic Scenes Through Anisoplanatic Turbulence," *IEEE Transactions on Computational Imaging*, vol. 6, pp. 1415–1428, 2020.
- [9] T. J. Schulz, "Multiframe Blind Deconvolution of Astronomical Images," *JOSA A*, vol. 10, no. 5, pp. 1064–1073, 1993.
- [10] F. Sroubek and P. Milanfar, "Robust Multichannel Blind Deconvolution via Fast Alternating Minimization," *IEEE Transactions on Image Processing*, vol. 21, no. 4, pp. 1687–1700, 2011.
- [11] K. Dabov, A. Foi, V. Katkovnik, and K. Egiazarian, "Image Denoising by Sparse 3-D Transform-Domain Collaborative Filtering," *IEEE Transactions on Image Processing*, vol. 16, no. 8, pp. 2080–2095, 2007.
- [12] R. Yasarla and V. M. Patel, "Learning to Restore a Single Face Image Degraded by Atmospheric Turbulence Using Cnns," *ArXiv Preprint ArXiv:2007.08404*, 2020. [Online]. Available: <https://arxiv.org/pdf/2007.08404>
- [13] ———, "Learning to Restore Images Degraded by Atmospheric Turbulence Using Uncertainty," in *2021 IEEE International Conference on Image Processing (ICIP)*, IEEE. IEEE, 2021, pp. 1694–1698.
- [14] C. P. Lau, H. Souri, and R. Chellappa, "ATFaceGAN: Single Face Image Restoration and Recognition From Atmospheric Turbulence," *2020 15th IEEE International Conference on Automatic Face and Gesture Recognition (FG 2020)*, pp. 32–39, 2020.
- [15] Z. Mao, N. Chimitt, and S. H. Chan, "Accelerating Atmospheric Turbulence Simulation Via Learned Phase-to-Space Transform," in *Proceedings of the IEEE/CVF International Conference on Computer Vision*, 2021, pp. 14759–14768.
- [16] P. Wieschollek, M. Hirsch, B. Scholkopf, and H. Lensch, "Learning Blind Motion Deblurring," in *Proceedings of the IEEE International Conference on Computer Vision*, 2017, pp. 231–240.
- [17] A. Bora, A. Jalal, E. Price, and A. G. Dimakis, "Compressed Sensing Using Generative Models," in *International Conference on Machine Learning*, PMLR. PMLR, 2017, pp. 537–546.
- [18] Y. Wu, M. Rosca, and T. Lillicrap, "Deep Compressed Sensing," in *International Conference on Machine Learning*, PMLR. PMLR, 2019, pp. 6850–6860.
- [19] F. Latorre, V. Cevher *et al.*, "Fast and Provable Admm for Learning With Generative Priors," *Advances in Neural Information Processing Systems*, vol. 32, pp. 12027–12039, 2019.
- [20] J. Whang, Q. Lei, and A. Dimakis, "Compressed Sensing With Invertible Generative Models and Dependent Noise," in *NeurIPS 2020 Workshop on Deep Learning and Inverse Problems*, 2020.
- [21] A. Jalal, L. Liu, A. G. Dimakis, and C. Caramanis, "Robust Compressed Sensing of Generative Models," *ArXiv Preprint ArXiv:2006.09461*, 2020. [Online]. Available: <https://arxiv.org/pdf/2006.09461>
- [22] G. Daras, J. Dean, A. Jalal, and A. G. Dimakis, "Intermediate Layer Optimization for Inverse Problems Using Deep Generative Models," *ArXiv Preprint ArXiv:2102.07364*, 2021. [Online]. Available: <https://arxiv.org/pdf/2102.07364>
- [23] P. Hand, O. Leong, and V. Voroninski, "Phase Retrieval Under a Generative Prior," *Advances in Neural Information Processing Systems*, 2018.
- [24] Z. Liu, S. Ghosh, and J. Scarlett, "Towards Sample-Optimal Compressive Phase Retrieval With Sparse and Generative Priors," *Advances in Neural Information Processing Systems*, vol. 34, 2021.
- [25] C. A. Metzler and G. Wetzstein, "Deep S³PR: Simultaneous Source Separation and Phase Retrieval Using Deep Generative Models," in *IEEE International Conference on Acoustics, Speech and Signal Processing*, IEEE. IEEE, 2021, pp. 1370–1374.
- [26] P. Hand and B. Joshi, "Global Guarantees for Blind Demodulation With Generative Priors," *Advances in Neural Information Processing Systems*, 2019.
- [27] D. Ren, K. Zhang, Q. Wang, Q. Hu, and W. Zuo, "Neural Blind Deconvolution Using Deep Priors," in *Proceedings of the IEEE/CVF Conference on Computer Vision and Pattern Recognition*, 2020, pp. 3341–3350.
- [28] M. Asim, F. Shamshad, and A. Ahmed, "Blind Image Deconvolution Using Deep Generative Priors," *IEEE Transactions on Computational Imaging*, vol. 6, pp. 1493–1506, 2020.
- [29] E. Bostan, R. Heckel, M. Chen, M. Kellman, and L. Waller, "Deep Phase Decoder: Self-Calibrating Phase Microscopy With an Untrained Deep Neural Network," *Optica*, vol. 7, no. 6, pp. 559–562, Jun 2020. [Online]. Available: <http://www.osapublishing.org/optica/abstract.cfm?URI=optica-7-6-559>
- [30] J. Liang, K. Zhang, S. Gu, L. Van Gool, and R. Timofte, "Flow-Based Kernel Prior With Application to Blind Super-Resolution," in *Proceedings of the IEEE/CVF Conference on Computer Vision and Pattern Recognition*, 2021, pp. 10601–10610.
- [31] J. W. Goodman, *Introduction to Fourier Optics*, 3rd ed. Englewood, Colo: Roberts & Co., 2005.
- [32] R. J. Noll, "Zernike Polynomials and Atmospheric Turbulence," *Journal of the Optical Society of America*, vol. 66, pp. 207–211, 1976.
- [33] N. Chimitt and S. H. Chan, "Simulating Anisoplanatic Turbulence by Sampling Correlated Zernike Coefficients," in *2020 IEEE International Conference on Computational Photography (ICCP)*, IEEE. IEEE, 2020, pp. 1–12.

- [34] I. Gulrajani, F. Ahmed, M. Arjovsky, V. Dumoulin, and A. C. Courville, “Improved Training of Wasserstein GANs,” in *Advances in Neural Information Processing Systems*, ser. NeurIPS 2017, 2017.
- [35] D. P. Kingma and J. Ba, “Adam: a Method for Stochastic Optimization,” *CoRR*, vol. abs/1412.6980, 2015.
- [36] A. Paszke *et al.*, “PyTorch: An Imperative Style, High-Performance Deep Learning Library,” in *Advances in Neural Inf. Process. Systems*, vol. 32, 2019.
- [37] T. Karras, S. Laine, and T. Aila, “A Style-Based Generator Architecture for Generative Adversarial Networks,” *2019 IEEE/CVF Conference on Computer Vision and Pattern Recognition (CVPR)*, pp. 4396–4405, 2019.
- [38] O. Russakovsky, J. Deng, H. Su, J. Krause, S. Satheesh, S. Ma, Z. Huang, A. Karpathy, A. Khosla, M. S. Bernstein, A. C. Berg, and L. Fei-Fei, “ImageNet Large Scale Visual Recognition Challenge,” *International Journal of Computer Vision*, vol. 115, pp. 211–252, 2015.
- [39] K. He, X. Zhang, S. Ren, and J. Sun, “Delving Deep into Rectifiers: Surpassing Human-Level Performance on ImageNet Classification,” *2015 IEEE International Conference on Computer Vision (ICCV)*, pp. 1026–1034, 2015.
- [40] D. Roich, R. Mokady, A. H. Bermano, and D. Cohen-Or, “Pivotal Tuning for Latent-Based Editing of Real Images,” *ArXiv Preprint ArXiv:2106.05744*, 2021.
- [41] Z. Liu, P. Luo, X. Wang, and X. Tang, “Deep Learning Face Attributes in the Wild,” in *Proceedings of International Conference on Computer Vision (ICCV)*, December 2015.
- [42] E. Agustsson and R. Timofte, “NTIRE 2017 Challenge on Single Image Super-Resolution: Dataset and Study,” *2017 IEEE Conference on Computer Vision and Pattern Recognition Workshops (CVPRW)*, pp. 1122–1131, 2017.
- [43] K. Hille, “Hubble Space Telescope Images,” Jan 2015. [Online]. Available: https://www.nasa.gov/mission_pages/hubble/multimedia/index.html
- [44] “CVPR 2022 UG2 Challenge Track 3 Atmospheric Turbulence Mitigation,” http://cvpr2022.ug2challenge.org/dataset22_t3.html, accessed: 2022-05-30.

APPENDIX A
PROOF OF THEOREM III.1

The following provides a proof for Theorem III.1, which states that by matching the distributions of the observed and simulated measurements, adversarial sensing will reconstruct the Fourier magnitude of \mathbf{x} accurately at all frequencies where the power spectral density of the blur kernels is non-zero.

Proof. If two random vectors have the same distribution, then their Fourier transforms will have the same distribution. Thus, if

$$p_{h*x}(\mathbf{y}) = p_{h*\tilde{x}}(\mathbf{y}), \quad (11)$$

then

$$p_{H \circ X}(\mathbf{Y}) = p_{H \circ \tilde{X}}(\mathbf{Y}), \quad (12)$$

where H , X , \tilde{X} , and Y denote the Fourier transforms of h , x , \tilde{x} , and y respectively. (Recall that convolution in the spatial domain is equivalent to elementwise multiplication in the spatial frequency domain.)

Random variables with the same distributions have the same absolute moments, therefore we have that

$$\mathbb{E}[|H \circ X|^2] = \mathbb{E}[|H \circ \tilde{X}|^2]. \quad (13)$$

This implies

$$X^2 \circ \mathbb{E}[|H|^2] = \tilde{X}^2 \circ \mathbb{E}[|H|^2]. \quad (14)$$

Equation (14) implies

$$X^2(K_u, K_v) = \tilde{X}^2(K_u, K_v) \quad \forall (K_u, K_v) \quad (15)$$

$$\text{s.t. } \mathbb{E}[|H|^2](K_u, K_v) \neq 0. \quad (16)$$

Let S denote a frequency domain mask with entries equal to 0 at spatial frequencies (K_u, K_v) where the power spectral density of h is 0, and with entries equal to 1 everywhere else. That is,

$$S(K_u, K_v) = \begin{cases} 1, & \text{if } \mathbb{E}[|H|^2](K_u, K_v) > 0, \\ 0, & \text{otherwise.} \end{cases} \quad (17)$$

We can now concisely represent condition (15) with the expression

$$S \circ X^2 = S \circ \tilde{X}^2, \quad (18)$$

which implies

$$S \circ |X| = S \circ |\tilde{X}|. \quad (19)$$

□

PROOF OF COROLLARY III.1.1

The following provides a proof for Corollary III.1.1, which states that if, in addition to assuming $p_{h*x}(\mathbf{y}) = p_{h*\tilde{x}}(\mathbf{y})$, one assumes $\mathbb{E}[\mathcal{F}\mathbf{h}](K_u, K_v) \neq 0$ for all spatial frequencies (K_u, K_v) , then one will successfully reconstruct \mathbf{x} .

Proof. If two random vectors have the same distribution, then their Fourier transforms will have the same distribution. Thus, if

$$p_{h*x}(\mathbf{y}) = p_{h*\tilde{x}}(\mathbf{y}), \quad (20)$$

then

$$p_{H \circ X}(\mathbf{Y}) = p_{H \circ \tilde{X}}(\mathbf{Y}), \quad (21)$$

where \mathbf{H} , \mathbf{X} , $\tilde{\mathbf{X}}$, and \mathbf{Y} denote the Fourier transforms of \mathbf{h} , \mathbf{x} , $\tilde{\mathbf{x}}$, and \mathbf{y} respectively.

Random variables with the same distributions have the same moments, therefore we have that

$$\mathbb{E}[\mathbf{H} \circ \mathbf{X}] = \mathbb{E}[\mathbf{H} \circ \tilde{\mathbf{X}}], \quad (22)$$

which implies

$$\mathbb{E}[\mathbf{H}] \circ \mathbf{X} = \mathbb{E}[\mathbf{H}] \circ \tilde{\mathbf{X}}. \quad (23)$$

We have assumed that $\mathbb{E}[\mathbf{H}](K_u, K_v) \neq 0$ for all spatial frequencies (K_u, K_v) , thus (23) implies $\mathbf{X} = \tilde{\mathbf{X}}$, which implies $\mathbf{x} = \tilde{\mathbf{x}}$. \square

APPENDIX B PSNR VALUES FOR FIG. 2

Typical	Lucky	Mao et al.	Ours-Face	Ours-IN	Ours-DIP
19.05	16.90	22.07	30.54	24.09	27.10
22.10	19.60	24.80	27.77	24.31	24.98
21.06	17.28	23.40	26.87	22.17	24.83
23.04	19.88	26.61	30.96	26.83	29.92

TABLE I: Rows ordered as in Fig. 2.

APPENDIX C PSNR VALUES FOR FIG. 3

Typical	Lucky	Mao et al.	Ours-Face	Ours-IN	Ours-DIP
22.80	20.86	25.10	24.27	24.58	25.73
18.33	13.96	21.57	24.91	20.67	24.88
11.76	9.96	13.08	14.88	13.64	22.43
14.15	12.10	17.12	15.30	19.81	19.66
16.67	13.99	19.29	23.65	19.15	26.82

TABLE II: Rows ordered as in Fig. 3.